

UNCLASSIFIED

Defense Technical Information Center
Compilation Part Notice

ADP012850

TITLE: Transition from Coherent to Incoherent Superlattices Transport

DISTRIBUTION: Approved for public release, distribution unlimited

Availability: Hard copy only.

This paper is part of the following report:

TITLE: Nanostructures: Physics and Technology International Symposium
[6th] held in St. Petersburg, Russia on June 22-26, 1998 Proceedings

To order the complete compilation report, use: ADA406591

The component part is provided here to allow users access to individually authored sections of proceedings, annals, symposia, etc. However, the component should be considered within the context of the overall compilation report and not as a stand-alone technical report.

The following component part numbers comprise the compilation report:

ADP012712 thru ADP012852

UNCLASSIFIED

Transition from coherent to incoherent superlattices transport

E. Gornik, C. Rauch and G. Strasser

Institut für Festkörperelektronik, Technische Universität Wien, Austria

Abstract. Ballistic electron transport is used to study the transmittance of GaAs/GaAlAs superlattices. In a three terminal transistor type device an energy tunable electron beam is injected via a tunneling barrier into an undoped superlattice. The transmitted current is measured as a function of the injector energy. Resonances in the collector current are observed due to miniband conduction in the GaAs/AlGaAs superlattice. By analysing the transfer ratio of superlattices at various bias conditions miniband positions and miniband widths are determined. A significant decrease of the miniband transmission is observed with increasing electric field across the superlattice, which is attributed to the quenching of coherent transport. For longer superlattices an asymmetry between positive and negative bias is found which is assigned to the transition between coherent and incoherent transport.

Introduction

Electron transport in superlattice minibands was first considered by Esaki and Tsu [1]. In their model they calculate the dispersion relation of the miniband determined by classical transport. In the quantum mechanical picture a voltage drop over the superlattice causes the break up of the miniband into a Wannier-Stark ladder [2], which requires a different description in terms of tunneling [3-4]. The tunneling current decreases with increasing electric field as the wavefunctions become localized. In the calculation of the current through an infinite superlattice a phenomenological scattering time has to be introduced to reproduce the onset of the negative differential conductivity at ω_B . $\tau = 1$, in order to mimic realistic current voltage characteristics [1, 5, 6] and thus the presence of incoherent transport.

A large number of studies of electrical transport in superlattices was done in the last decade [7–10]. In short period superlattices the formation of allowed and forbidden bands for resonant tunneling and band filling effects were confirmed experimentally [11-12]. The study of biased superlattices was severely hindered by space charge built up and domain formation [13]. So far there is no conclusive experiment which shows the occurrence of Esaki-Tsu type negative differential resistance (RTD) due to Bragg reflection at the zone boundary. Sybille et al. [14-15] performed the most extensive study in biased, doped superlattices and observed negative differential velocity. They were able to fit the drift velocity-voltage curves by using a modified Esaki-Tsu drift diffusion model.

Optical experiments led to a breakthrough by the observation of Bloch oscillations in the time domain of undoped superlattices [16]. In a previous experiment we have developed a three terminal technique which allowed the study of transport in undoped superlattices [17]. In this paper, we extend this technique of hot electron spectroscopy to biased superlattices [18].

Experimental

We measured ballistic transport in GaAs/Ga_{0.7}Al_{0.3}As superlattices, where the influence of electron-electron and electron-impurity scattering can be neglected due to extremely low current densities. Under flat band conditions the eigenstates of the periodic structure are extended over the entire length of the superlattice. To investigate the superlattice properties, a hot electron transistor structure is used. An energy tunable electron beam is generated by a tunneling emitter, passes the superlattice after traversing a thin highly doped GaAs region (base) and an undoped drift region. Electrons passing the superlattice are collected in a doped GaAs layer, reflected electrons are collected by the base contact.

Our samples, grown by molecular beam epitaxy, have the following common features: A highly doped n⁺-GaAs collector contact layer is grown on a semi-insulating GaAs substrate. Followed by a superlattice and the drift regions which are slightly n-doped ($\sim 5 \times 10^{14} \text{ cm}^{-3}$), in order to avoid undesired band bending. To reduce quantum mechanical confining effects originating from the quantum well formed by the emitter barrier and the superlattice the drift region is chosen to be at least 200 nm in width. This is followed by a highly doped ($2 \times 10^{18} \text{ cm}^{-3}$) n⁺-GaAs layer (base) of 13 nm width. As found in previous experiments [19], about 75% of the injected electrons traverse the base ballistically. On top of the base layer a 13 nm undoped Ga_{0.7}Al_{0.3}As barrier is grown followed by a spacer and a n⁺-GaAs layer, nominally doped to $n = 3 \times 10^{17} \text{ cm}^{-3}$, in order to achieve an estimated normal energy distribution of injected electrons of about 20 meV [20]. Finally, a n⁺-GaAs contact layer ($n = 1 \times 10^{18} \text{ cm}^{-3}$) is grown on top of the heterostructure to form the emitter.

Standard photolithographic and wet etching techniques were employed in three terminal device processing. The emitter, base, and collector were contacted from above using a standard AuGe/Ni alloy. An emitter contact pad, which is connected to the $30 \times 30 \mu\text{m}$ emitter mesa, is evaporated on top of a polyimide isolation layer.

Results and discussion

Before we start to investigate the transmittance of the superlattice minibands, we want to have an exact knowledge of the energy distribution of the injected electrons. Thus, a three terminal device with a resonant tunneling diode instead of the superlattice was used to determine the shape of the injector. The energy diagram of the conduction band of this device is shown in Fig. 1. A resonant tunneling diode acts as an energy filter of the injected hot electrons. Electrons that have an energy which corresponds to the energy of the first resonant state can pass the energy filter, otherwise they are scattered back to the base and do not contribute to the measured collector current. The RTD (6 nm Al_{0.3}Ga_{0.7}As barrier/12 nm GaAs well/8 nm Al_{0.3}Ga_{0.7}As barrier) is designed in a way that the first state (23 meV) is well below the energy of an LO-phonon ($\hbar\omega_{\text{LO}} = 36 \text{ meV}$) in order not be influenced by electrons that are scattered by LO-phonons. The measured ballistic current is in the order of $1 \mu\text{A}/\text{cm}^2$.

The measured transfer ratio as a function of the injection energy, which is equivalent to the applied negative emitter bias, is shown in Fig. 2. Below the energy of the first resonant state E_1 of the RTD we observe no collector current, since no electrons are injected that have an energy which is high enough to cross the resonant tunneling barrier. The onset at about 21 meV determines the energy level of the first resonant state

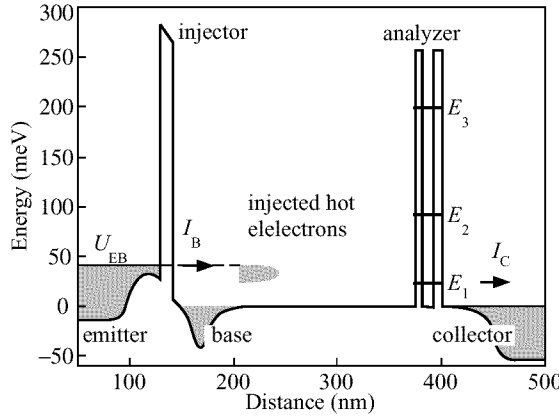


Fig 1. Schematic band diagram of a three terminal device with a resonant tunneling diode as a filter to measure the injected electron distribution.

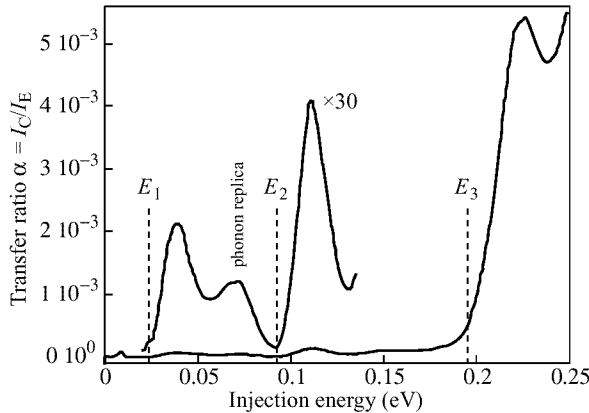


Fig 2. The transfer ratio $\alpha = I_C/I_E$ versus injection energy of the three terminal device with RTD. For injection energies up to 130 meV the transfer ratio is multiplied by a factor of thirty. The resonant states of the analyzer are indicated by dashed lines. LO-phonon replicas are observed for all levels.

(E_1) of the analyzer RTD. By further increasing the emitter bias, we use the constant energy position of the first resonant state to perform spectroscopy of the injected hot electron distribution. Because the resonant linewidth of the double barrier structure is negligible compared to the width of the injector distribution, the measured transfer ratio is proportional to the hot electron distribution of the injector. The observed second peak at about 70 meV is due to electrons that are injected at higher energy and have lost 36 meV due to LO-phonon emission during transversing the base layer and the drift region. Since the k-vector in the current direction is conserved for LO-phonon scattering processes, these electrons are also collected efficiently at higher injection energies. The transfer ratio does not drop to zero in between these peaks due to the overlap of the injected electron distributions that traverse the drift region without scattering and those electrons that have lost the LO-phonon energy. Starting at about 90 meV we observe transport through the second resonant state (E_2). This peak reproduces the shape of

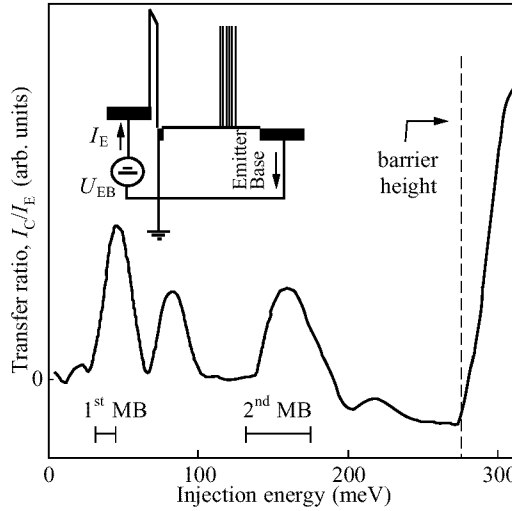


Fig 3. The transfer ratio $\alpha = I_C/I_E$ versus injection energy ($\approx e \cdot U_{EB}$) of a sample with a 8.5 nm GaAs/2.5 nm AlGaAs superlattice. The calculated miniband positions are indicated by bars (|—|). The inset shows the measurement circuit in the common-base configuration.

the injected electron distribution for higher injection energies. At 187 meV we observe the third quantized level of the RTD. It should be noted that the measured onsets of the transfer ratio fits very well to the calculated positions of the position of the quantized states ($E_{1,calc} = 23$ meV, $E_{2,calc} = 87$ meV, and $E_{3,calc} = 179$ meV). The calculated positions are indicated by dashed lines in Fig. 2.

Since the first peak of the transfer ratio is proportional to the injected hot electron energy distribution we can determine the full width at half maximum to be 20 meV. The shape of the distribution is slightly asymmetric with its maximum at the high energy side with respect to the GaAs conduction band edge. We observe no significant change of the shape of the energy distribution with higher injection energies up to 200 meV.

The static transfer ratio $\alpha = I_C/I_E$, of a 8.5 nm/2.5 nm GaAs/AlGaAs five period superlattice is plotted in Fig. 3 as a function of the injection energy. Several maxima and a sharp rise at 280 meV are observed. The inset in Fig. 3 shows the measurement circuit used for the determination of the transfer ratio. All measurements are performed in common base configuration at 4.2 K. No current is observed below the energy of the first peak. The position of the first peak coincides very well with the first miniband. Thus, we conclude that the first peak is due to miniband transport through the lowest miniband. For energies higher than the first miniband the transfer ratio drops quite significantly since there is no transport possible through the forbidden minigap of the SL. The second observed peak is shifted 36 meV to higher injection energies and is attributed to the first LO-phonon emission replica ($\hbar\omega_{LO} = 36$ meV) of the injected electron distribution. The relative position in energy and width are equal to that of the first peak. The energy range of electrons injected at voltages corresponding to these second peak is in the forbidden band and no contribution is expected from electrons which have not lost energy due to optical phonon emission. The peak at 150 meV represents transport through the second SL miniband. For an analysis of the observed features we compare the experimental data with the theoretically calculated miniband

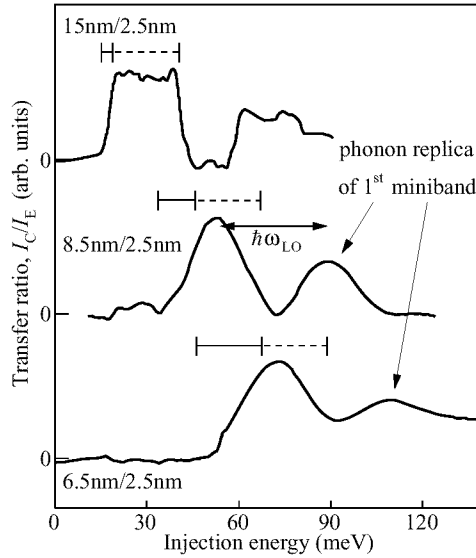


Fig 4. Transfer ratio I_C/I_E versus injection energy at lower injection energies for three samples with different superlattices (—|—| indicates the calculated miniband position, |— —| indicates the broadening due to the energy distribution of the injected electron beam). A double arrow represents the energy of a longitudinal optical phonon ($\hbar\omega_{LO} = 36$ meV).

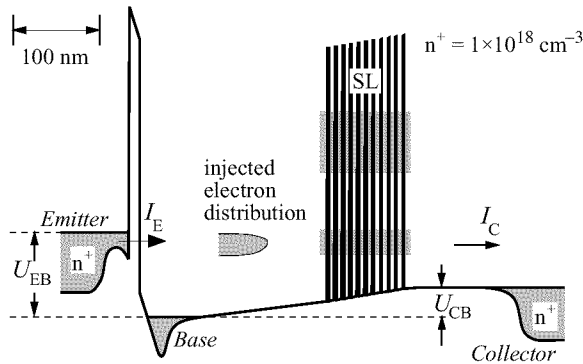


Fig 5. Schematic band diagram of a three terminal device with negative bias applied to the superlattice. The miniband positions are indicated by shaded areas. The base is grounded.

positions. The calculated positions and widths of the first and second miniband are indicated by bars. The sharp rise of the transfer ratio at 280 meV is due to the transition to continuum. This energy, which corresponds to the conduction band offset of the superlattice barriers, gives us a confirmation for the AlAs mole fraction of the AlGaAs compound.

In Fig. 4 we show the transfer ratio a as a function of the injection energy for three samples all have five periods with different well widths at low injection energies. There is a clear shift of the peaks to higher energies with decreasing superlattice well width. The calculated miniband positions are again indicated by bars as in Fig. 3. Since the calculated miniband width for the widest well is 3.5 meV and the observed peak

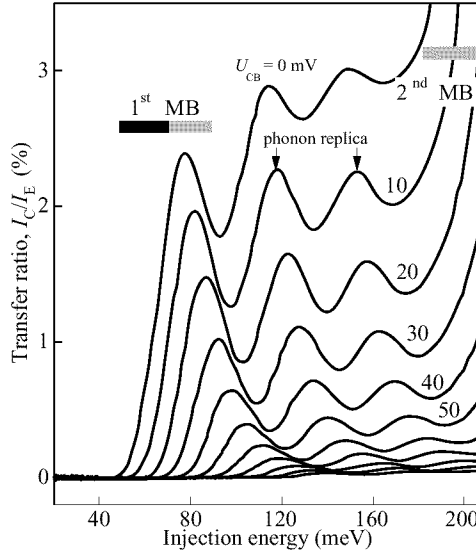


Fig 6. Transfer ratio α vs. injection energy at different collector base voltages. The dark bars indicate the calculated position of the minibands. The gray bars represents the full width at half maximum of the injected electron energy distribution.

corresponding to miniband transport through the first miniband has a width of about 24 meV, we can confirm the initial energy distribution of the injector to be about 20 meV wide, in agreement with the results shown in Fig. 2.

The measurements on biased superlattices are performed on a superlattice consisting of 5 and 10 periods of nominally 2.5 nm thick $\text{Al}_{0.3}\text{Ga}_{0.7}\text{As}$ barriers and 6.5 nm GaAs wells. For these parameters a simple Kronig-Penney calculation gives one miniband lying between 46 meV and 68 meV, and a second one between 182 meV and 276 meV. The calculated equilibrium Γ -point conduction energy diagram including band bending is shown in Fig. 5 for typical biasing conditions.

Fig. 6 shows a set of measured transfer ratios as a function of electron injection energy at different collector biases. As long as the injection energy is lower than the first miniband no ballistic current is observed. The sharp increase of the transfer ratio at about 45 meV coincides with the lower edge of the first miniband. The onset of the transfer ratio (miniband transport) shifts with the applied collector-base bias since the lower edge of the first miniband shifts with the applied bias. The value of the electric field in the superlattice is determined from a comparison of the measured miniband position (using the 3 dB criterium) with the miniband position derived from a self consistent Schrödinger calculation of the entire structure.

Longitudinal optical phonon replicas, shifted by 36 meV to higher injection energies, are observed at all biases and are used as an additional calibration for the applied bias. Due to these phonon replicas the transfer ratio does not vanish between the peaks since the full width at half maximum of the injected electron distribution (20 meV) plus the width of the first miniband (22 meV) is greater than the phonon energy. At zero bias the transmission through the superlattice should have a maximum, if we assume that the electronic wave functions of all superlattice states are extended over the total dimension

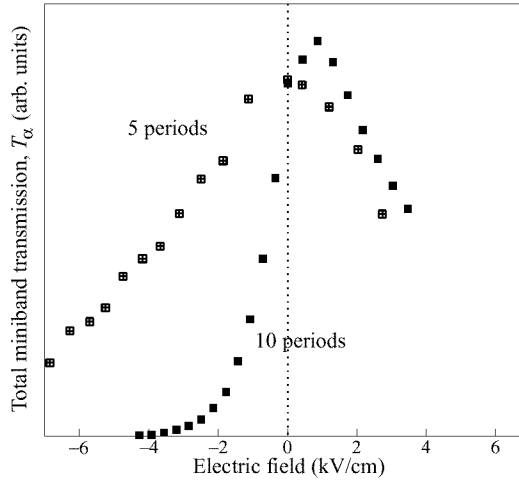


Fig 7. Measured total miniband transmission vs applied electric field.

of the superlattice.

The total miniband transmission, as a measure of the transmission, is defined as the integral over the first half of transfer ratio as a function of bias of the first peak. This represents the transport through the first miniband not taking into account electrons which have lost an LO phonon. Fig. 7 shows the total miniband transmission versus electric field for two different superlattices. It can be seen that the transmission vanishes for an applied electric field exceeding 4 kV/cm and 8 kV/cm. For low electric fields the superlattice states extend successively one after the other over the total superlattice dimension and become transparent which leads to an increase of current. At zero bias most of the superlattice states are extended, leading to a maximum of the measured transmission.

If we now compare the transmission for the five and ten period superlattice as a function of positive and negative bias we find clear differences: while the transmission for the five period superlattice is symmetric and independent of the bias direction the ten period superlattice shows a clear asymmetry. This asymmetry we assign to the onset of scattering in the ten period superlattice. This is also consistent with the assumption that the mean free path is in the order of 800 nm in our samples which is just longer than the five period and shorter than the ten period superlattice.

Summary

In summary direct experimental current spectroscopy of minibands in undoped superlattices is demonstrated using the technique of Hot Electron Spectroscopy. Miniband transport through the first and second miniband of superlattices with different well widths as a function of the hot electron injection energy is observed. We measured the injected electron distribution and are able to determine miniband widths and positions for flatband conditions. The obtained miniband widths and positions agree very well with theoretical calculations. The structure described in this paper gives the highest energy resolution reported so far.

Additionally we have shown the controlled decrease of superlattice conduction in a

superlattice with bias using the technique of hot electron spectroscopy. The experimental results are in good agreement with a calculation based on a transfer matrix method.

Acknowledgement

This work was partly supported by the Austrian Federal Ministry of Science, the Society for Microelectronics (GMe, Austria), and the U.S. Army European Research Office.

References

- [1] L. Esaki, and R. Tsu, *IBM J. Res. Dev.* **14** 61 (1970).
- [2] G. H. Wannier, *Elements of Solid State Theory* (Cambridge University Press, London, 1959), pp. 190-193.
- [3] R. Tsu and L. Esaki, *Appl. Phys. Lett.* **22** 562 (1973).
- [4] J.B. Krieger and G.J. Iafrate, *Phys. Rev. B* **33** 5494 (1986).
- [5] R.A. Suris and B.S. Shchamkhalova, *Sov. Phys. Semicond.* **18** 738 (1984).
- [6] R. Tsu, and G. Döhler, *Phys. Rev. B* **12** 680 (1975).
- [7] L. Esaki and L.L. Chang, *Phys. Rev. Lett.* **33** 495 (1974).
- [8] F. Beltram, F. Capasso, D.L. Sivco, A.L. Hutchinson, S.-N.G. Chu, and A.Y. Cho, *Phys. Rev. Lett.* **64** 3167 (1990).
- [9] P. Voisin, J. Bleuse, C. Bouche, S. Gaillard, C. Alibert, and A. Regreny, *Phys. Rev. Lett.* **61** 1639 (1988); J. Bleuse, P. Voisin, M. Allovon, and M. Quilicq, *Appl. Phys. Lett.* **53** 2632 (1988).
- [10] E.E. Mendez, F. Agullí-Ruada, and J.M. Hong, *Phys. Rev. Lett.* **60** 2426 (1988).
- [11] P. England, M. Helm, J.R. Hayes, J.P. Harbison, E. Colas, and L.T. Florez, *Appl. Phys. Lett.* **54** 647 (1989).
- [12] G. Brozak, M. Helm, F. DeRosa, C.H. Perry, M. Koza, R. Bhat and S.J. Allen, *Phys. Rev. Lett.* **64** 3163 (1990).
- [13] H.T. Grahn, R.J. Haug, W. Müller, K. Ploog, *Phys. Rev. Lett.* **67** 1618 (1991).
- [14] A. Sibille, J.F. Palmier, H. Wang, F. Molloy, *Phys. Rev. Lett.* **64** 52 (1990).
- [15] A. Sibille, J.F. Palmier, F. Molloy, *Appl. Phys. Lett.* **60** 52 (1992).
- [16] Ch. Waschke, H.G. Roskos, R. Schwedler, K. Leo, H. Kurz, and K. Köhler, *Phys. Rev. Lett.* **70** 3319 (1993).
- [17] C. Rauch, G. Strasser, K. Unterrainer, B. Brill, and E. Gornik, *Appl. Phys. Lett.* **70** 649 (1997).
- [18] C. Rauch, G. Strasser, K. Unterrainer, W. Boxleitner, E. Gornik, *phys. stat. sol. (b)* **204** 393 (1997).
- [19] B. Brill, to be published (1996).
- [20] S. Bending, A. Peck, J. Leo, K.v. Klitzing, P. Gueret, and H.P. Meier, *Solid-State Electronics* **32** 1161 (1989).